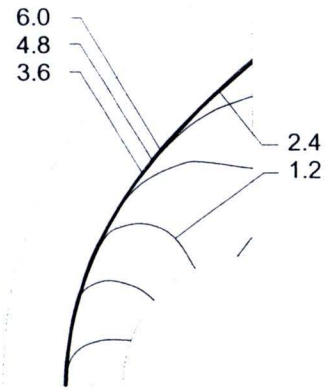

รูปที่ 7 แสดงเส้นชั้นค่ามัคนัมเบอร์ของการไหลแบบไม่หนืด
ด้วยความเร็วกว่าเสียง 6.47 เท่าผ่านทรงกระบอก

เอกสารอ้างอิง

1. Dechaumphai, P. and Weitng, A.R. "Coupled Fluid–Thermal–Structural Analysis for Aerodynamically Heated Structures," Finite Element Analysis in Fluids, edited by T.J. Chung and G.R. Karr, Univ. of Alabama in Huntsville Press, Huntsville, AL, April 1989, pp. 165–171.
2. Zienkiewicz, O.C., Lohner, R., and Morgan, K. "High–Speed Inviscid Compressible Flow by the Finite Element Method," 5th MAFELAP Conference, Brunel University, May, 1984.
3. Limtrakarn, W. and Dechaumphai, P. "An Explicit Finite Element Method for Inviscid Compressible Flow," Proceedings of the 15th Conference of the Mechanical Engineering Network of Thailand, 2001.
4. Lohner, R., Morgan, K. Peraire, J. and Vahdati, M. "Finite Element Flux–Corrected Transport (FEM–FCT) for the Euler and Navier–Stokes Equations," ICASE report, No. 87–4.
5. Peraire, J., Vahdati, M., Morgan, K., and Zienkiewicz, O.C. "Adaptive Remeshing for Compressible Flow Computation," Journal of Computational Physics, 72, 1987.
6. Ramakrishnan, R., Bey, K.S., and Thornton, E.A. "Adaptive Quadrilateral and Triangular Finite Element Schemes for Compressible Flows," AIAA Journal 1,1990.
7. Gnoffo, P.A. "Application of Program LAURA to Three–Dimensional AOTV Flowfields," AIAA–86–0565, pp.1-12.

8. Giraldo, F. "A Finite Volume High Resolution 2D Euler Solver with Adaptive Grid Generation on High Performance Computers," 9th International Conference on Finite Elements in Fluids, 1995.
9. Limtrakarn, W. and Dechaumphai, P. "Computations of High–Speed Compressible Flows with Adaptive Cell–Centered Finite Element Method," Journal of the Chinese Institute Engineers, 26, 2003.
10. Moss, J.N. "DSMC Simulation of Shock Interactions about Sharp Double Cones," NASA TM–210318, 2000.
11. Holden, M.S., Wadhams, T.P., Harvey, J.K., and Candler, G.V. "Comparisons between DSMC and Navier–Stokes Solutions on Measurements in Regions of Laminar Shock Wave Boundary Layer Interaction in Hypersoics Flows," AIAA paper 2002–0435.
12. Pandolfi, M., D'Ambrosio, D. "Numerical Instabilities in Upwind Methods: Analysis and Cures for the Carbuncle Phenomena," Journal of Computational Physics, 166(2), 2001, pp. 271–301.
13. Dechaumphai, P. and Phongthanapanich, S. "High–Speed Compressible Flow Solutions by Adaptive Cell–Centered Upwinding Algorithm with Modified H–Correction Entropy Fix," Advanced Engineering Software, 34(9), 2003, pp. 533–538.
14. Kim, K.H., Kim, C., Rho, O.H. "Methods for the Accurate Computations of Hypersonic Flows: I. AUSMPW+ Scheme," Journal of Computational Physics, 174(1), 2001, pp. 38–40.
15. Lomtev, I. and Karniadakis, G. E. "A Discontinuous Galerkin Method for the Navier–Stokes Equations, " InternationalJournal for Numerical Methods in Fluids, 29, 1999, pp. 587–603.
16. Cockburn, B., Luskin, Mitchell, Shu, C. W., and Suli, E. "Enhanced Accuracy by Post–Processing for Finite Element Methods for Hyperbolic Equations," Math. Comput., 72(242), 2003, pp. 577–606.
17. Tu, S. and Aliabadi, S. "A Slope Limiting Procedure in Discontinuous Galerkin Finite Element Method for Gas Dynamics Applications", Int. J. of Numerical Analysis and Modeling, 2(2), 2005, pp. 163 – 178.
18. Huebner, K. H.; Thornton, E. A.; Byrom, T. G. The Finite Element Method for Engineers. 3rd ed. New York : John Wiley & Sons, 1995.
19. Timoshenko, S. P. and Goodier, J. N. Theory of Elasticity. 3rd ed. Singapore : McGrawHill International Editions.

สรุปและวิจารณ์ผล

งานวิจัยนี้เป็นศึกษาและวิเคราะห์ปัญหาการไหลอัดตัวได้แบบไม่หนืดใน 2 มิติ ด้วยวิธีกาเลอร์คินแบบไม่ต่อเนื่อง ร่วมกับเทคนิคการปรับขนาดเอลิเมนต์โดยอัตโนมัติ ทำให้คำตอบที่ได้มีความแม่นยำ ช่วยลดเวลาและหน่วยความจำในการคำนวณ โดยมีการตรวจสอบความถูกต้องของโปรแกรมกาเลอร์คินแบบไม่ต่อเนื่องกับผลเฉลยแม่นตรง โปรแกรมที่พัฒนาขึ้นสามารถนำไปประยุกต์ปัญหาที่มีความซับซ้อนได้ เช่น ปัญหาการไหลความเร็วสูงกว่าเสียง 6.47 เท่า ผ่านทรงกระบอก เป็นต้น

ข้อเสนอแนะสำหรับงานวิจัยในอนาคต

1. พัฒนาวิธีกาเลอร์คินแบบไม่ต่อเนื่องกับปัญหาการไหลอัดตัวได้แบบหนืดใน 2 มิติ
2. พัฒนาวิธีกาเลอร์คินแบบไม่ต่อเนื่องกับปัญหาการไหลความเร็วต่ำใน 2 มิติ

Output จากโครงการวิจัยที่ได้รับทุนจาก สกว.

1. **Limtrakarn, W.**, Yodsangkham, A., Namlaow, A., and Dechaumphai, P., "Determination of *KI, KII* and Trajectory of Initial Crack by Adaptive Finite Element Method and Photoelastic Technique", Experimental Techniques, doi: 10.1111/j.1747–1567.2009.00527.x, 2009, pp. 27 – 35. (Impact factor = 0.4)

ภาคผนวก

by W. Limtrakarn, A. Yodsangkham, A. Namlaow, and P. Dechaumphai

DETERMINATION OF K_I, K_{II} AND TRAJECTORY OF INITIAL CRACK BY ADAPTIVE FINITE ELEMENT METHOD AND PHOTOELASTIC TECHNIQUE

Life prediction of single or multi-material products is one of the most important studies in engineering design and maintenance. Crack propagation speed and its trajectory are the key behaviors to assess the life of products. Determination of the stress intensity factors on crack tip are needed to accurately predict the crack propagation and its trajectory. Several numerical methods and nondestructive experimental techniques are currently being used to determine such phenomena. The photoelastic technique with an optic-experimental interference has been employed to determine the stress intensity factors and the crack's trajectories.[1–4] Its principle is based on the double refraction phenomenon by analyzing the maximum shear stress induced in the transparent or birefringent of the photoelastic model under loading. The phenomenon is observed by looking through the optical elements, i.e. the polarizer and the analyzer of the polariscope, as demonstrated in Fig. 1. Their results provide information that can be applied directly to metal prototypes by using the law of similarity. At present, several numerical methods have also been developed to predict crack propagation phenomenon. These methods include the finite element method,[5–7] the meshless method,[8,9] the manifold method with virtual crack extension,[10] and the boundary element method.[11]

In this paper, the stress intensity factors K_I and K_{II}, including the trajectory of the initial crack, are determined using the adaptive finite element method and the photoelastic technique. The theory of the two-dimensional fracture mechanics is described first. The finite element method using the 8-node quadrilateral elements surrounding the crack tip together with the adaptive meshing technique are explained. The finite element formulation and its computational procedure are described. The photoelastic technique is then presented for determining the stress intensity factors. The maximum circumferential stress theory is used to calculate the trajectory of the initial crack. Both the finite element method and the photoelastic technique are evaluated by benchmark problems. The first two problems are the single-edge cracked plate and the double-edge cracked plate under tensile loading. Their results obtained from the adaptive finite element method and the photoelastic technique are compared with those presented by Brown.[12] The third problem is the slant-edge cracked plate subjected to uniform tensile loading. Both the finite element method and the photoelastic technique solutions are compared with the empirical formula of Murakami[13] for different crack length ratios.

W. Limtrakarn (Limwiroj@tu.ac.th) is a lecturer and A. Yodsangkham, and A. Namlaow are graduate students in the Department of Mechanical Engineering Faculty of Engineering, Thammasat University, Rungsit Campus, Pathumthani, Thailand. P. Dechaumphai is a lecturer in the Department of Mechanical Engineering, Faculty of Engineering, Chulalongkorn University, Bangkok, Thailand.

doi: 10.1111/j.1747-1567.2009.00527.x

THEORY

Stress and Stress Intensity Factor Relations

The relations of the stress and the stress intensity factors for modes I and II using the Linear Elastic Fracture Mechanics (LEFM) theory are,[14]

$$\sigma_x = \frac{1}{\sqrt{2\pi r}}\left[K_I \cos\tfrac{\theta}{2}\left(1-\sin\tfrac{\theta}{2}\sin\tfrac{3\theta}{2}\right) - K_{II}\sin\tfrac{\theta}{2}\left(2+\cos\tfrac{\theta}{2}\cos\tfrac{3\theta}{2}\right)\right] \quad (1)$$

$$\sigma_y = \frac{1}{\sqrt{2\pi r}}\left[K_I \cos\tfrac{\theta}{2}\left(1-\sin\tfrac{\theta}{2}\sin\tfrac{3\theta}{2}\right) + K_{II}\sin\tfrac{\theta}{2}\cos\tfrac{\theta}{2}\cos\tfrac{3\theta}{2}\right] \quad (2)$$

$$\tau_{xy} = \frac{1}{\sqrt{2\pi r}}\left[K_I \sin\tfrac{\theta}{2}\cos\tfrac{\theta}{2}\cos\tfrac{3\theta}{2} + K_{II}\cos\tfrac{\theta}{2}\left(1-\sin\tfrac{\theta}{2}\sin\tfrac{3\theta}{2}\right)\right] \quad (3)$$

where K_I and K_{II} are the stress intensity factors for the opening mode (mode I) and the tearing mode (mode II); r and θ are the distance and the angle in the polar coordinates as shown in Fig. 2; σ_x and σ_y are the normal stresses in x and y directions, respectively, and τ_{xy} is the shearing stress.

The general form of the stress intensity factor at the crack tip is given by,[15]

$$K = F\sigma_\infty\sqrt{\pi a} \quad (4)$$

where F is the geometry factor that depends on the dimensions of problem, σ_∞ is the far-field stress, and a is the crack length.

The stress intensity factors K_I and K_{II} can be computed from displacement extrapolation near the crack tip. These stress intensity factors are expressed by,

$$K_I = \frac{E}{3(1+\nu)(1+\kappa)}\sqrt{\frac{2\pi}{L}}\left(4(v_b - v_d) - \left(\frac{v_c - v_e}{2}\right)\right) \quad (5)$$

$$K_{II} = \frac{E}{3(1+\nu)(1+\kappa)}\sqrt{\frac{2\pi}{L}}\left(4(u_b - u_d) - \left(\frac{u_c - u_e}{2}\right)\right) \quad (6)$$

where E is the modulus of elasticity, ν is the Poisson's ratio, κ is the elastic parameter defined by $(3-4\nu)$ for plane strain case and $(3-\nu)/(1+\nu)$ for plane stress case, L is the element length, and u and v are the displacement components in x and y directions, respectively. The subscripts of u and v represent their positions for the nodes of the elements surrounding the crack tip as shown in Fig. 3(a). Figure 3(b) provides detail of the 8-node quadrilateral element with their mid-side node positions, while nodes 1, 4, and 8 are collapsed and placed together at the crack tip.

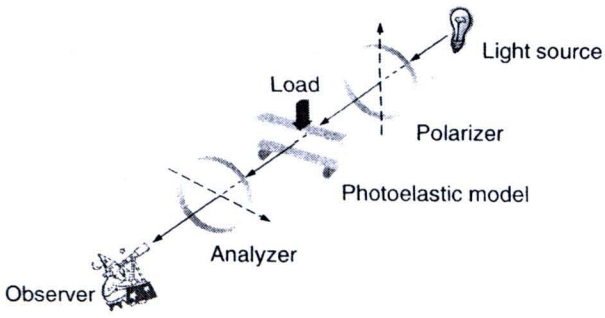

Fig. 1: Photoelastic model under loading in a polariscope

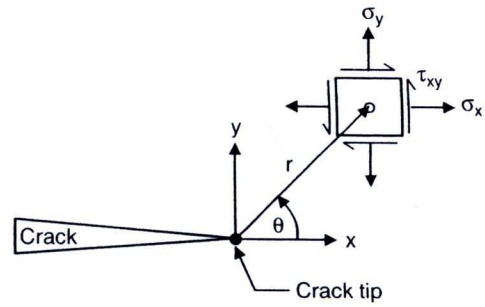

Fig. 2: State of stresses in polar coordinates from crack tip

Crack propagation in two-dimensional fracture mechanics problems is normally caused by mixed mode loading. Several methods are employed to predict the trajectory of initial crack. These methods have been developed using the maximum circumferential stress theory,[16] the maximum energy release rate theory,[17] and the minimum strain energy density method.[18] In the maximum circumferential stress theory, the direction of crack propagation θ_p is computed from,

$$K_I \sin\theta_p + K_{II}(3\cos\theta_p - 1) = 0 \tag{7}$$

where θ_p is determined from,

$$\theta_p = 2\tan^{-1}\left(\frac{\frac{K_I}{K_{II}} \pm \sqrt{\left(\frac{K_I}{K_{II}}\right)^2 + 8}}{4}\right) \tag{8}$$

Equation 7 implies that the crack propagates at zero angle, θ_p, for the pure mode I, and at a nonzero angle for the case of mixed mode loading.

Finite Element Method

The finite element equations can be derived from the governing differential equations of equilibriums. The derived

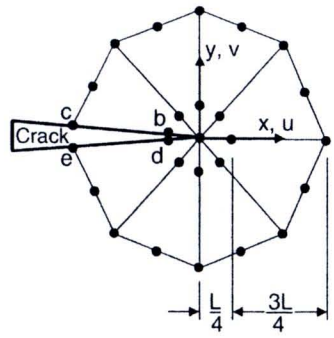

(a) Quarter–point quadrilateral elements around crack tip

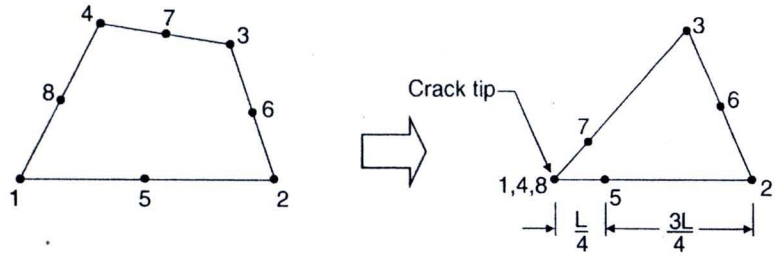

(b) A quarter–point eight–node quadrilateral element.

Fig. 3: Eight-node quadrilateral element around crack tip

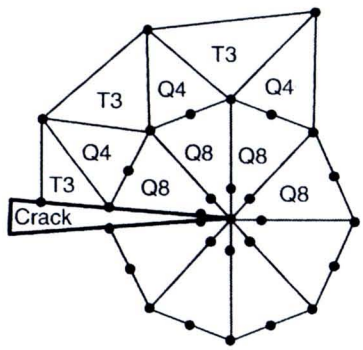

Fig. 4: Combination of three element types surrounding crack tip

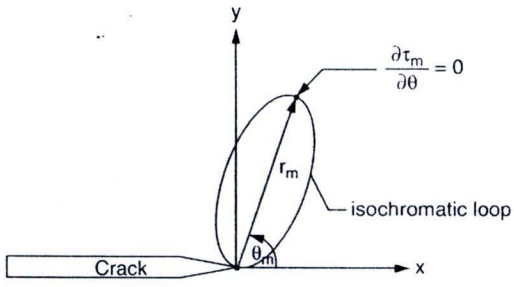

Fig. 5: Distance r_m and angle θ_m of isochromatic loop

finite element equations are written in matrix form as,

$$[K]\{\delta\} = \{F\} \tag{9}$$

where $\{\delta\}$ is the vector of the element nodal displacements, $[K]$ is the element stiffness matrix,[19] and $\{F\}$ is the element load vector.

To obtain a solution with good accuracy around the crack tip, the finite elements with high-order element interpolation functions are preferred. The eight-node quadrilateral elements (Q8) are selected herein to construct a circular zone surrounding the crack tip. These elements have their mid-side nodes displaced from their nominal position to quarter points of the tip as shown in Fig. 3(a). The radius of the circular zone is specified to be no longer than one-eight of the initial crack length, with roughly one element every 30° in the circumferential direction.[20]

The four-node quadrilateral elements (Q4) are also chosen to connect the Q8 elements at the crack tip with the triangular elements (T3) in the regions away from the crack tip as shown in Fig. 4.

Photoelastic Technique

The reflection photoelastic technique can be used to determine the state of stresses and crack speed on transparent material under both the static and dynamic conditions.[21] The technique provides the relationships of the

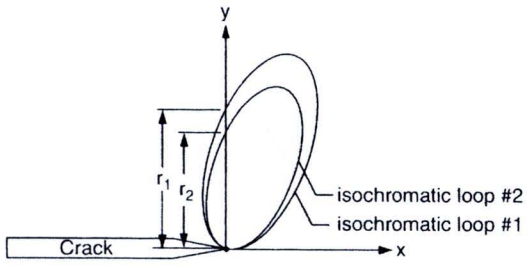

Fig. 6: Distance r_m of two isochromatic loops

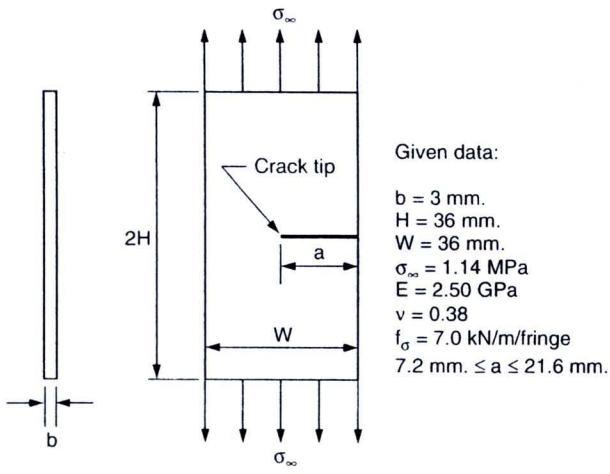

Fig. 7: Problem statement of single-edge cracked plate under tensile loading

direct isochromatic fringe pattern and the difference of the principle stresses as,

$$\sigma_1 - \sigma_2 = 2\tau_m = \frac{Nf_\sigma}{2t} \tag{10}$$

where τ_m is the maximum inplane shear stress, f_σ is the stress-optical constant, N is the order of the isochromatic fringe, and t is the thickness of specimen.

The maximum shear stress is related with the stress components in the form,

$$(2\tau_m)^2 = (\sigma_x - \sigma_y)^2 + 4\tau_{xy}^2 \tag{11}$$

Similarly, by substituting Eqs. 1–3 into Eq. 11, the relationship between the maximum shear stress and the stress intensity factors is obtained,[22]

$$\begin{aligned}(2\tau_m)^2 = {} & \tfrac{1}{2\pi r}\left[(K_I \sin\theta + 2K_{II}\cos\theta)^2 + (K_{II}\sin\theta)^2\right] \\ & + \tfrac{2}{\sqrt{2\pi r}} \sin\tfrac{\theta}{2}\left[K_I \sin\theta(1 + 2\cos\theta)\right] \\ & + K_{II}(1 + 2\cos^2\theta + \cos\theta)\end{aligned} \tag{12}$$

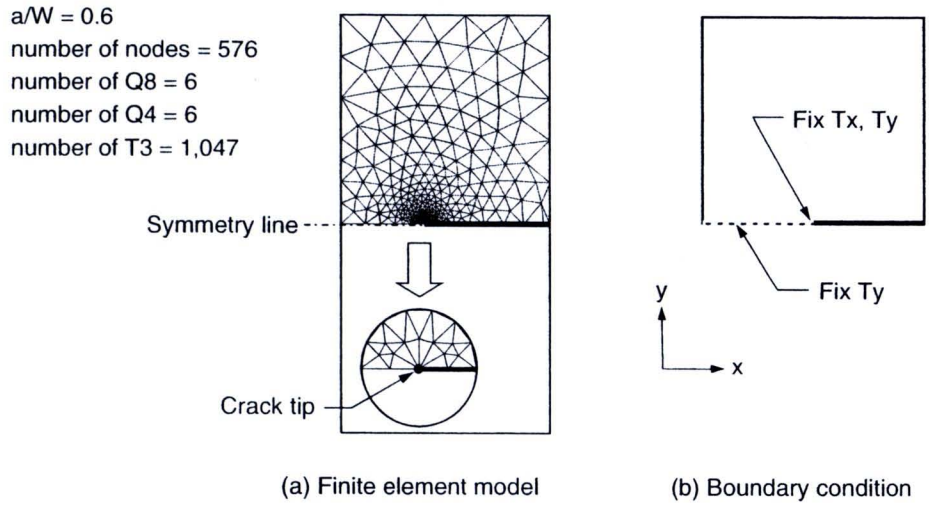

Fig. 8: Adaptive finite element model of single-edge cracked plate with a/W = 0.6

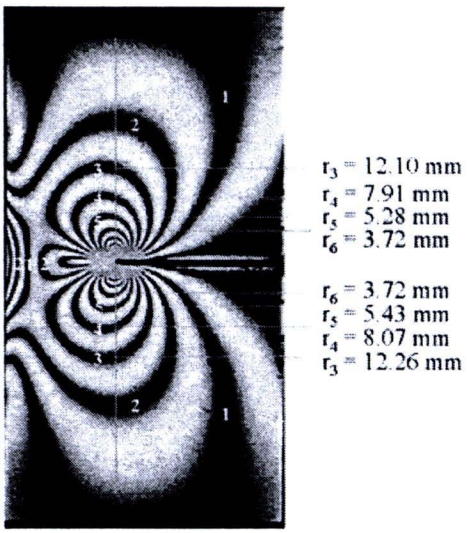

Fig. 9: Photoelastic result of single-edge cracked plate with a/W = 0.6

Similarly, by substituting Eq. 10 into Eq. 12, the stress intensity factor for the opening mode can be expressed in the form,

$$K_I = \frac{Nf_\sigma}{2t}\frac{\sqrt{2\pi r_m}}{\sin\theta_m}\left[1+\left(\frac{2}{3\tan\theta_m}\right)^2\right]^{-\frac{1}{2}} \left(1+\frac{2\tan\frac{3\theta_m}{2}}{3\tan\theta_m}\right) \quad (13)$$

where θ_m is the angle of inclination to the crack plane and r_m is the distance from crack tip to the farthest point on a given isochromatic loop as shown in Fig. 5. The position of the farthest point on a given isochromatic loop is represented by $\partial\tau_m/\partial\theta = 0$.

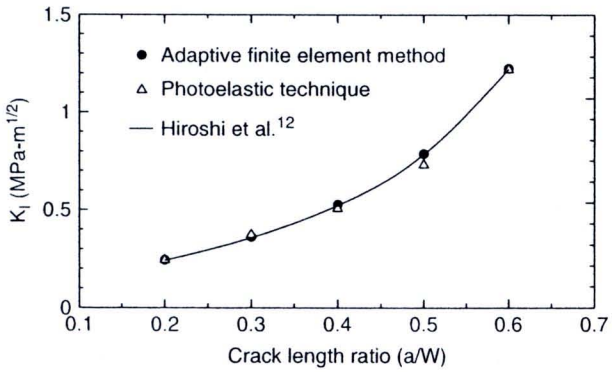

Fig. 10: Comparative stress intensity factor K_I for single-edge cracked plate

The relationship between the stress intensity factors and the angle θ_m is obtained by minimizing Eq. 12 with respect to θ to yield,

$$\left(\frac{K_{II}}{K_I}\right)^2 - \frac{4}{3}\left(\frac{K_{II}}{K_I}\right)\cot 2\theta_m - \frac{1}{3} = 0 \quad (14)$$

Equation 14 above is used to determine the ratio (K_{II}/K_I) by measuring the angle θ_m on the isochromatic loop which is valid at the point very close to the crack tip. The direction of crack propagation θ_p can then be computed by substituting the ratio (K_{II}/K_I) into Eq. 8. By using the measured data from the two isochromatic loops along the line perpendicular to the crack plane $(\theta = 90^\circ)$[23] as shown in Fig. 6, the stress intensity factor can be computed from,[22]

$$K_I = \frac{f_\sigma}{2t}\sqrt{2\pi r_1}\frac{(N_1 - N_2)}{1-\sqrt{(r_1/r_2)}} \quad (15)$$

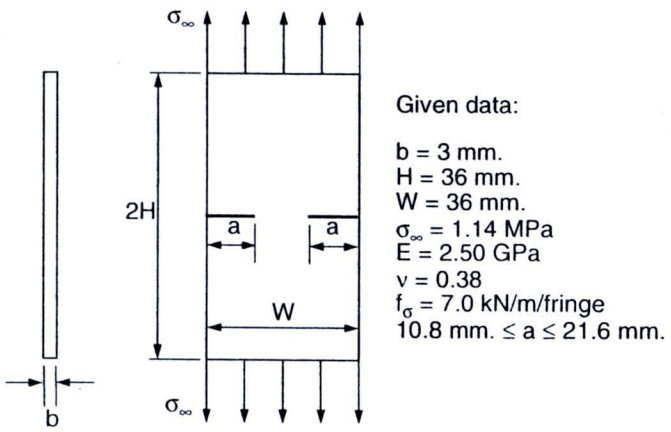

Fig. 11: Problem statement of double-edge cracked plate under tensile loading

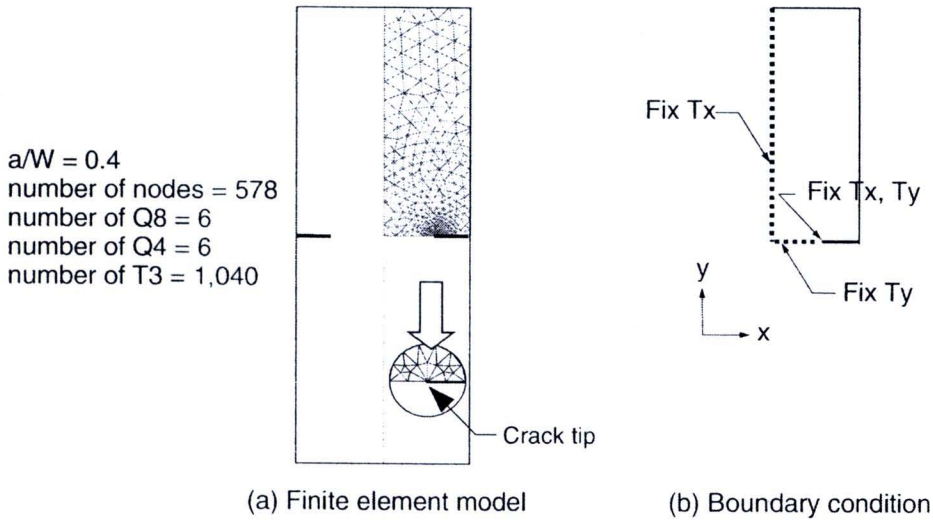

Fig. 12: Adaptive finite element model of double-edge cracked plate in tension with a/W = 0.4

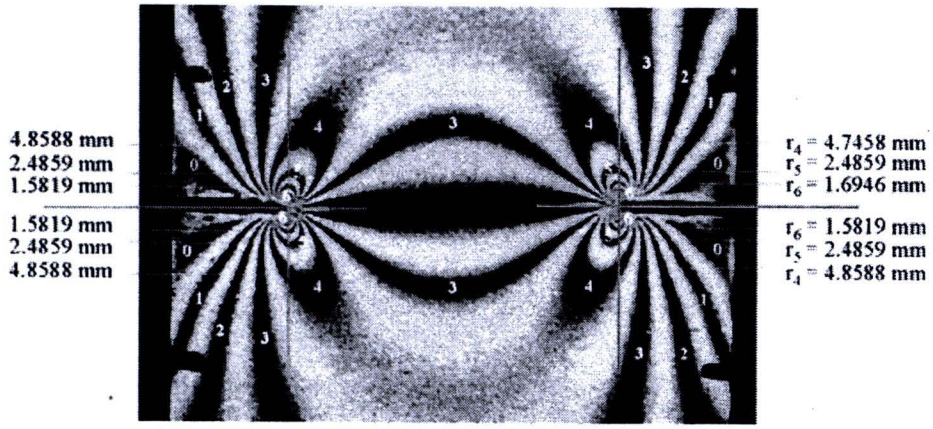

Fig. 13: Photoelastic result of double-edge cracked plate in tension with a/W = 0.4

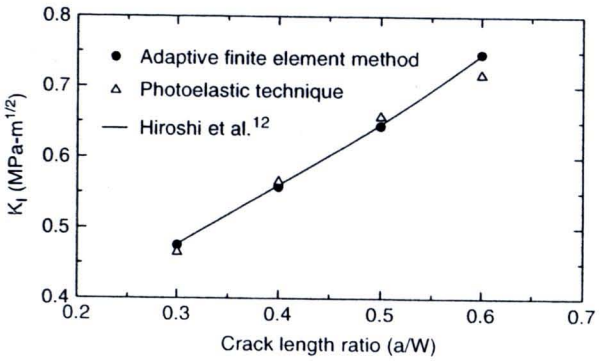

Fig. 14: Comparative stress intensity factors for double-edge cracked plate

APPLICATIONS

The adaptive finite element method and the photoelastic technique are evaluated by using the three benchmark problems of: (1) the single-edge cracked plate, (2) the double-edge cracked plate, and (3) the slant-edge cracked plate, all under uniaxial tensile loading. Results are compared with those presented by Hiroshi et al.[12] and Murakami.[13] All plates have dimensions of 36 × 72 × 3 mm and are made from polycarbonate material for which one side is coated with resin and diethylenetriamine with silver color. Isopropyl alcohol is required to degrease and clean the coating surfaces.

Single-Edge Cracked Plate

A rectangular plate has varied crack length per width (a/W) between 0.2 to 0.6. The plate is subjected to a far-field tensile stress of $\sigma_\infty = 1.14$ MPa along the top and bottom edges as shown in Fig. 7. Due to symmetry of the problem, only the upper half of the plate is used as a finite element model. Five analysis cases were performed with the crack length per width of 0.2, 0.3, 0.4, 0.5, and 0.6. As an example for the case with the crack length per width of 0.6, the adaptive finite element mesh containing six Q8-elements, six Q4-elements, and 1047 of the T3 elements, with the total of 576 nodes, is shown in Fig. 8.

It is noted that the stress intensity factor given by Hiroshi et al.[12] for this problem is,

$$K_I = \sigma_\infty \sqrt{\pi a}\left[1.122 - 0.231\frac{a}{W} + 10.55\left(\frac{a}{W}\right)^2 - 21.71\left(\frac{a}{W}\right)^3 + 30.382\left(\frac{a}{W}\right)^4\right] \quad (16)$$

The computed stress intensity factor for the opening mode K_I obtained from the adaptive finite element method and the photoelastic technique is 1.22410 and 1.22271, as compared to 1.22074 from Eq. (16) with the differences of 0.28 and 0.16%, respectively.

Figure 9 shows the photoelastic result using the photo camera technique[22] for the case of a/W = 0.6. The measured values of r_i for each N_i, $i = 1$–4, for the top and bottom fringe images are used to calculate the average stress intensity factors.

Results of the stress intensity factor K_I from the finite element method and the photoelasticity technique are compared with those given by Hiroshi et al. for the five cases of a/W = 0.2, 0.3, 0.4, 0.5, and 0.6 as shown in Fig. 10. The figure shows good agreement of the solutions for all cases of the crack length ratio.

Double-Edge Cracked Edge Plate

The geometry and material properties of a double-edge cracked plate under tensile loading is shown in Fig. 11.

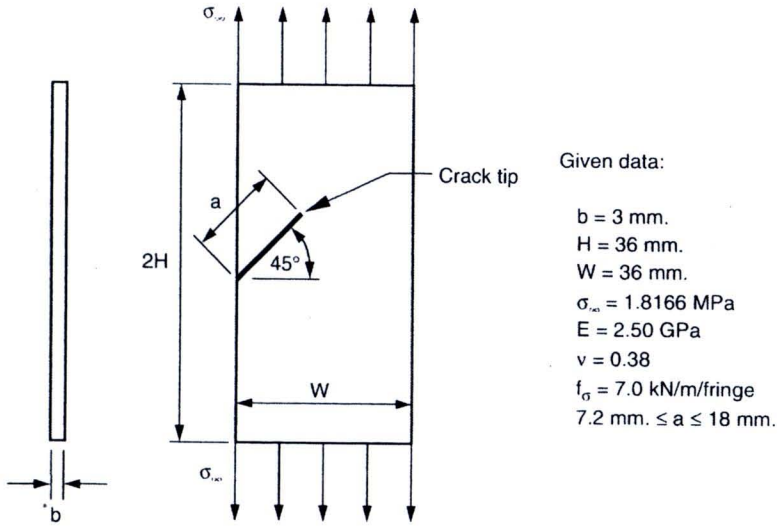

Fig. 15: Problem statement of slant-edge cracked plate under tensile loading

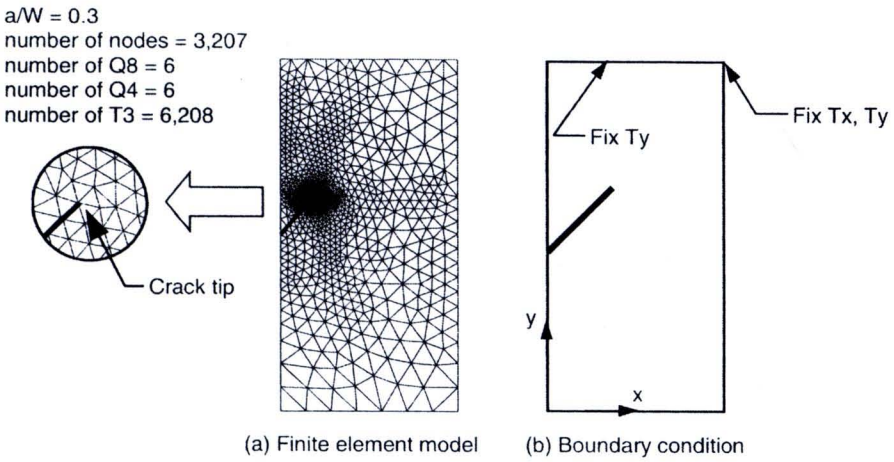

Fig. 16: Adaptive finite element model of slant-edge cracked plate with a/W = 0.3

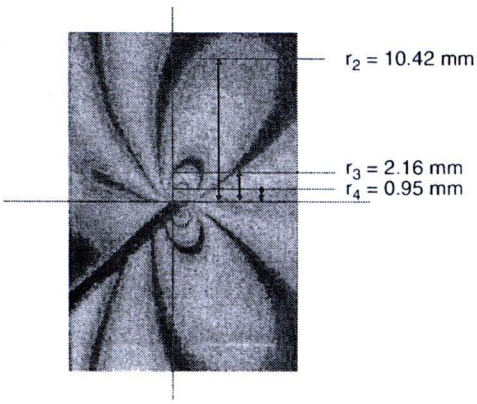

Fig. 17: Photoelastic result of slant-edge cracked plate with a/W = 0.3

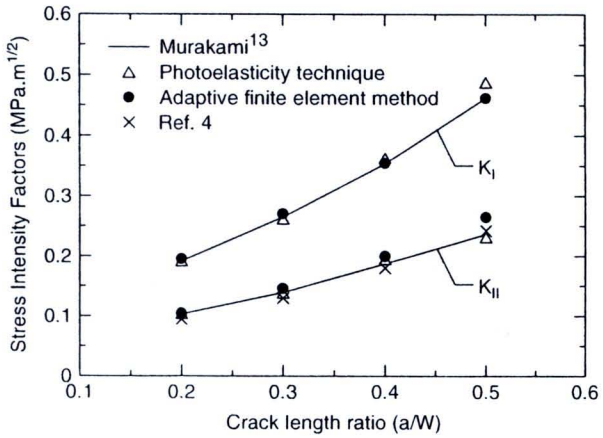

Fig. 18: Comparing stress intensity factors of slant-edge cracked plate

The plate has two cracks in the middle of both sides, with the crack length ratio that varies from 0.3 to 0.6. Due to symmetry of the problem, only the upper right quarter of the plate can be used for finite element modeling.

Figure 12 shows the final adaptive finite element model for the case of a/W = 0.4. This finite element model consists of 578 nodes with 6 Q8 elements, 6 Q4 elements, and 1040 of the T3 elements. The stress intensity factor for opening mode K_I of this problem is given by,[12]

$$K_I = \sigma_\infty \sqrt{\pi a}\left[1.122 - 0.561\frac{a}{W} - 0.015\left(\frac{a}{W}\right)^2 - 0.091\left(\frac{a}{W}\right)^3\right] \Big/ \sqrt{1-\frac{a}{W}} \qquad (17)$$

The photoelastic fringe image for the case of a/W = 0.4 recorded by the polariscope is shown in Fig. 13. By selecting the distances r_4, r_5, and r_6 of isochromatic fringe image as

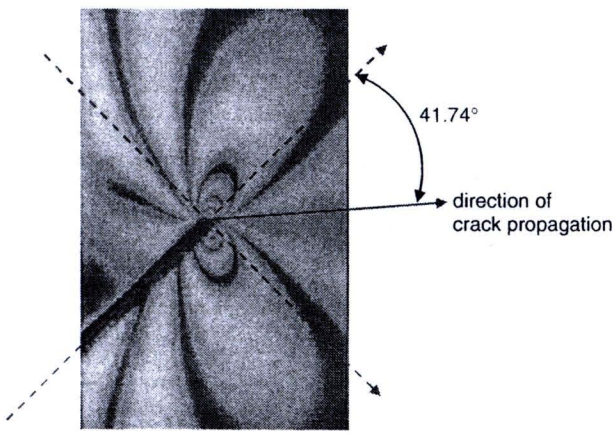

Fig. 19: Direction of crack propagation for slant-edge cracked plate with a/W = 0.3

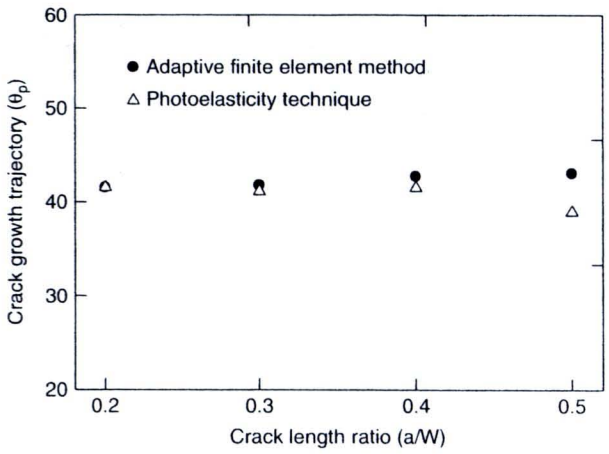

Fig. 20: Comparative trajectories of initial crack for slant-edge cracked plate

shown in the figure, the average stress intensity factor is computed using Eq. 15.

Figure 14 shows the results of the stress intensity factors obtained from the finite element method and the photoelastic technique as compared to that from Eq. 17. The figure shows good agreement of the finite element method and the photoelastic technique with the average differences of 0.26 and 2.19%, respectively.

Slant-Edge Cracked Plate

The geometry and material properties of the plate in this example are the same as the previous one. The crack has a 45° inclined angle with the horizontal line as shown in Fig. 15. Under tensile loading, σ_∞, an inclined crack with mixed mode occurs. Figure 16 shows the adaptive finite element mesh with 3207 nodes, 6 Q8 elements, 6 Q4 elements, and 6208 of the T3-elements.

The photoelastic fringe image for the case of a/W = 0.3 is shown in Fig. 17. The average stress intensity factor K_I is computed by measuring the distance r_m of the isochromatic fringe loop numbers 2, 3, and 4, and substituting them into Eq. 15. The stress intensity factor K_{II} is computed by measuring the angle θ_m on the isochromatic loop and substituting it into Eq. 14. Figure 18 shows good agreement of the computed stress intensity factors K_I and K_{II} of the mixed mode from adaptive finite element method, the photoelastic technique and that presented in Ref. 13. The average K_I differences of adaptive finite element method and the photoelastic technique results are 2.38 and 3.52%, respectively, from Ref. 13. Correspondingly, the average K_{II} differences of adaptive finite element method and the photoelastic technique results are 5.93 and 2.7%, respectively, from Ref. 13. By using the photoelastic technique with the substitution of K_I and K_{II} into Eq. 8, the crack propagation direction for the case of a/W = 0.3 is presented in Fig. 19. Figure 20 compares the crack growth trajectories between the adaptive finite element method and the photoelastic technique for all the four cases of $0.2 \leqslant a/W \leqslant 0.5$.

CONCLUSIONS

An adaptive finite element method using the eight-node quadrilateral finite element surrounding the crack tip is presented to analyze two-dimensional fracture mechanics problems. The method is used to determine the stress intensity factors and the trajectory of initial crack. The adaptive finite element method generates small elements in the crack region to capture high stress gradient for providing high solution accuracy. Larger elements are generated in the other regions where the stress gradients are small to reduce number of elements and thus the computational time. The reflection photoelastic technique is also employed to obtain the stress intensity factors. The benchmarks problems of: (1) single-edge cracked plate, (2) double-edge cracked plate, and (3) slant-edge cracked plate under tensile loading were used to evaluate the performance of the finite element method and the reflection photoelastic technique. Results obtained from the finite element method and the reflection photoelastic technique are compared by using the stress intensity factors. In the first example of the single-edge cracked plate, the differences of the stress intensity factor K_I obtained from the finite element method and the photoelastic technique from the Hiroshi et al. result[12] are 0.88 and 3.12%, respectively. These stress intensity factor differences are 0.26 and 2.19% for the second example of the double-edge cracked plate. In the third example of the slant-edge cracked plate, the stress intensity factors K_I and K_{II} obtained from the adaptive finite element method and the photoelastic technique also agree very well with those shown in Ref. 13. These examples have demonstrated the applicability and advantages of the adaptive finite element method for providing accurate prediction of the stress intensity factors, including the trajectory of initial crack.

ACKNOWLEDGEMENTS

The authors are pleased to acknowledge the Thailand Research Fund (TRF) for supporting this research work.

References

1. Gdoutos, E.E., Theocaris, P.S., "A Photoelastic Determination of Mixed-mode Stress-intensity Factors," *Experimental Mechanics* **18**(3):87–96, (1978).

2. Zhengmei, L., Ping, S., "Photoelastic Determination of Mixed-mode Stress-intensity Factors KI, KII, and KIII," *Experimental Mechanics* **23**(2):228–235, (1983).

3. Patterson, E.A., Olden, E.J., "Optical Analysis of Crack Tip Stress Fields: a Comparative Study," *Fatigue & Fracture of Engineering Materials and Structures* **27**(7):623–635, (2004).

4. Guagliano, M., Sangirardi, M., Vergani, L., "Photoelastic Methods to Determine KI, KII, and KIII of Internal Cracks Subjected to Mixed Mode Loading," *International Journal of Fatigue* **28**(5–6):576–582, (2006).

5. Kim, J.H., Paulino, G.H., "Simulation of Crack Propagation in Functionally Graded Materials under Mixed-mode and Non-proportional Loading," *International Journal of Mechanics and Materials in Design* **1**(63–94):(2004).

6. Phongthanapanich, S., Dechaumphai, P., "Adaptive Delaunay Triangulation with Object-oriented Programming for Crack Propagation Analysis," *Finite Element in Analysis and Design* **40**(13–14):1753–1771, (2004).

7. Alshoaibi, A.M., Hadi, M.S.A., Ariffin, A.K., "An Adaptive Finite Element Procedure for Crack Propagation Analysis," *Journal of Zheijang University Science A* **8**(2):228–236 (2006).

8. Rao, B.N., Rahman, S., "An Efficient Meshless Method for Fracture Analysis for Cracks," *Computational Mechanics* **26**:398–408 (2000).

9. Luliang, L., Pan, Z., "Meshless Method for 2D Mixed–mode Crack Propagation Based on Voronoi Cell," *ACTA Mechanica Solida Sinca* **16**(3):231–239, (2003).

10. Chiuo, Y.J., Lee, Y.M., Tsay, R.J., "Mixed Mode Fracture Propagation by Manifold Method." *International Journal of Fracture* **114**:327–347 (2002).

11. Xu, K., Lie, S.T., Cen, Z., "Crack Propagation Analysis with Galerkin Boundary Element Method," *International Journal for Numerical and Analytical Methods in Geomechanics* **22**(5):421–435, (2004).

12. Hiroshi, T., Paul, C.P., George, R.I., *The Stress Analysis of Crack Handbook*, ASME Press, New York (1985).

13. Murakami, Y., *Stress Intensity Factors, Volume 2*, Pergamon Press, New York (1986).

14. Anderson, T.L., *Fracture Mechanics: fundamentals and Applications*, CRC Press Boca Raton, FL (1994).

15. Limtrakarn, W., "Stress Analysis on Crack Tip Using Q8 and Adaptive Meshes," *Thammasat International Journal of Science and Technology*. **10**(1):19–24 (2005).

16. Erdogan, F., Sih, G.C., "On the Crack Extension in Plates under Plane Loading and Transverse Shear," Journal of Basic Engineering **85**:519–527 (1963).

17. Nuismer, R.J., "An Energy Release Rate Criterion for Mixed Mode Fracture," *International Journal of Fracture*. **11**(2):245–250 (1975).

18. Sih, G.C., "Strain–energy–density Factor Applied to Mixed Mode Crack Problems," *International Journal of Fracture*. **10**:305–321 (1974).

19. Zienkiewicz, O.C., Taylor, R.L., *Finite Element Method*, 5th Edition, Butterworth–Heinemann, Woburn (2000).

20. Guinea, G.V., Planas, J., Elices, M., "K Evaluation by the Displacement Extrapolation Technique." *Engineering Fracture Mechanics*. **66**(3):243–255, (2000).

21. Irwin, G.R., "Discussion of the Dynamic Stress Distribution Surrounding a Running Crack–A Photoelastic Analysis," *Proceedings of the Society of Experimental Stress Analysis* **16**(1):93–96, (1958).

22. Paipetis, S.A., Holister, G.S., *Photoelasticity in Engineering Practice*, Elsevier Applied Science Publishers, New York (1985).

23. Schroedl, M.A., Smith, C.W., "Local Stress Near Deep Surface Flaws under Cylindrical Bending Fields," *ASTM STP* **536**:45–63 (1973). ■